

Thermal photon emission from the $\pi\rho\omega$ system

Nathan P. M. Holt,^{*} Paul M. Hohler,[†] and Ralf Rapp[‡]
*Cyclotron Institute and Department of Physics & Astronomy,
Texas A&M University, College Station, Texas 77843-3366, USA*

We investigate thermal photon emission rates in hot hadronic matter from a system consisting of π , ρ , and ω mesons. The rates are calculated using both relativistic kinetic theory with Born diagrams as well as thermal field theory at the two-loop level. This enables us to cross-check our calculations and to manage a pole contribution that arises in the Born approximation corresponding to the $\omega \rightarrow \pi^0\gamma$ radiative decay. After implementing hadronic form factors to account for finite-size corrections, we find that the resulting photo-emission rates are comparable to existing results from $\pi\rho \rightarrow \pi\gamma$ processes in the energy regime of 1–3 GeV. We expect that our new sources will provide a non-negligible contribution to the total hadronic rates, thereby enhancing calculated thermal photon spectra from heavy-ion collisions, which could improve the description of current direct-photon data from experiment.

I. INTRODUCTION

One of the goals at the forefront of nuclear physics is to understand the phase diagram of strongly interacting matter [1, 2]. At sufficiently high temperatures, hadronic matter undergoes a transition from color-neutral particles to a quark-gluon plasma (QGP) with deconfined color charge. As this transition is believed to be a crossover, the properties of hadronic matter are expected to change continuously as temperatures approach the pseudo-critical one, $T_{pc} \approx 160$ MeV [3, 4]. The phases of QCD matter can be explored in ultra-relativistic heavy-ion collisions (URHICs) where a fireball of high-temperature strongly-interacting matter is created. This matter rapidly cools and ultimately decouples into confined particles which are then detected. Hadronic probes of the medium undergo strong rescattering and alterations while traversing the fireball thus losing direct information about the properties of the hot and dense phases of the evolution. Electromagnetic (EM) probes (photons and dileptons), on the other hand, are emitted throughout the evolution of the fireball, escaping relatively unaltered since their mean free path is much longer than the size of the fireball. They thus encode information on properties of the fireball which are not easily accessible otherwise, e.g., on its interior temperatures, the total space-time volume, and evolution history of its collective properties (see, e.g., the reviews in Refs. [5–7] for further information on the role of EM probes in URHICs).

Theoretical models of EM probes in URHICs relate dilepton and photon spectra to the properties of the emitting medium. The calculated emission spectra of dileptons [5, 8] agree well with experimental measurements thus far [9–11], while similar calculations of the photon spectra [12] indicate potential discrepancies with recent

measurements of direct photons [13–17]. This discrepancy concerns both the spectral yields and the photon elliptic flow (v_2).

Much theoretical effort has gone into addressing this putative “puzzle” [12, 18–28]. The tentative conclusion of most of these approaches is that there are currently unaccounted-for thermal photon sources from the strongly-interacting medium. The difficulty in the problem and the diversity in possible solutions comes from identifying these new sources. For example, additional sources from a hot QGP, which contribute early in the evolution, are disfavored as they carry a small v_2 (the fireball needs a time of the order of the nuclear size, $\tau_{FB} \sim R_A$, to build up the momentum anisotropy) and too hard of a spectral slope. This leads one to consider sources which contribute later in the fireball evolution as prime candidates for generating the necessary v_2 [12, 22, 24, 26].

The present paper aims at identifying such sources by investigating novel sources of photon production from hot hadronic matter, and in this way contribute to a more complete characterization of the electromagnetic emissivity of QCD matter in a regime of moderate temperatures. Specifically, we will explore photon emission rates from a thermally equilibrated system composed of π , ρ , and ω mesons, and put their relevance into context with existing rate calculations (alternatively our calculated scattering matrix elements can be used in transport simulations where the momentum distributions are not necessarily thermal). The coupling strength of the $\pi\rho\omega$ vertex, which is pivotal to our analysis, is known to be large [29, 30]. It was instrumental in identifying the ω t -channel exchange in the $\pi\rho \rightarrow \pi\gamma$ process as an important contributor to the photon emissivity of a hot meson gas [31] (and, in fact, to the $\omega \rightarrow \pi^0\gamma$ decay [32]). Thus, a more systematic analysis of pertinent processes, including the ω meson as an external particle (incoming or outgoing), is warranted. Since the ω is not a stable particle under strong interactions (it can decay into $\pi\rho$ or 3π), some care has to be taken when evaluating pertinent scattering diagrams. To ensure that this is done correctly, we calculate the emission rates using both kinetic theory

^{*}Electronic address: nathan.holt@physics.tamu.edu

[†]Electronic address: pmhohler@comp.tamu.edu

[‡]Electronic address: rapp@comp.tamu.edu

and thermal field theory techniques to identify potential issues and cross-check the results.

The remainder of this paper is organized as follows. In Sec. II, we briefly recapitulate two methods for calculating thermal photon production in the context of the $\pi\rho\omega$ system, including the specification of the interaction Lagrangians. In Sec. III, we calculate photo-emission rates using kinetic theory (KT) with Born scattering amplitudes. In Sec. IV, we use thermal field theory (TFT) to compute two-loop diagrams of the photon self-energy to both check the KT results and address some intricacies in the kinetic approach. In Sec. V, we present our results and compare them to existing hadronic photo-emission rates. We conclude in Sec. VI.

II. THERMAL PHOTON EMISSION RATES

The thermal photon production rate can be written as [33]

$$q_0 \frac{dR_\gamma}{d^3q} = -\frac{\alpha_{em}}{\pi^2} f(q_0, T) \text{Im} \Pi_{em}^T(q_0 = |\vec{q}|, T), \quad (1)$$

where q_0 and $|\vec{q}|$ are the photon's energy and three-momentum magnitude, respectively, and f is the thermal Bose-Einstein distribution function. Employing the vector meson dominance (VMD) model [34], the 3D-transverse part of the EM current-current correlator, Π_{em}^T , is proportional to the in-medium vector meson spectral function (dominated by the ρ meson) via

$$\Pi_{em}^T(q_0, \vec{q}) = \frac{(m_\rho^{(0)})^4}{g_\rho^2} D_\rho^T(q_0, \vec{q}), \quad (2)$$

with a dressed ρ propagator

$$D_\rho^T(q_0, \vec{q}) = \left[q_0^2 - |\vec{q}|^2 - (m_\rho^{(0)})^2 - \Sigma_\rho^T(q_0, \vec{q}) \right]^{-1}, \quad (3)$$

where $m_\rho^{(0)}$ is the bare ρ mass and Σ_ρ^T is the in-medium ρ self-energy. In the VMD model, the thermal photon emission calculation thus amounts to calculating the ρ meson self-energy, usually done using TFT.

Alternatively, calculations of thermal photon emission can be done using KT. In Ref. [35], it was shown that the imaginary parts of self-energies can be expressed as vacuum scattering amplitudes (i.e. using zero-width external particles) folded with appropriate thermal statistical weightings and integrated over the pertinent phase space. In this framework, the thermal photon emission rate is expressed in terms of a $1 + 2 \rightarrow 3 + \gamma$ scattering process given by

$$q_0 \frac{dR_\gamma}{d^3q} = \mathcal{N} \int \frac{d^3p_1}{(2\pi)^3 2E_1} \frac{d^3p_2}{(2\pi)^3 2E_2} \frac{d^3p_3}{(2\pi)^3 2E_3} \times (2\pi)^4 \delta^4(p_1 + p_2 - p_3 - q) |\overline{\mathcal{M}}|^2 \times f(E_1, T) f(E_2, T) \frac{[1 + f(E_3, T)]}{2(2\pi)^3}, \quad (4)$$

where \mathcal{N} is the combined spin and isospin degeneracy of the incoming particles and $|\overline{\mathcal{M}}|^2$ is the initial-state spin- and isospin-averaged scattering amplitude of the process under consideration.

The microscopic ingredients to the photo-emission rates using the above frameworks are the ρ self-energy (for TFT) and photon-producing scattering amplitudes (for KT). Both quantities can be derived on the same footing from an underlying interaction Lagrangian. We start with a Lagrangian for free π and ρ fields,

$$\mathcal{L}_\pi + \mathcal{L}_\rho = \frac{1}{2} \partial_\mu \vec{\pi} \cdot \partial^\mu \vec{\pi} - \frac{1}{2} m_\pi^2 \vec{\pi} \cdot \vec{\pi} - \frac{1}{4} \vec{\rho}_{\mu\nu} \cdot \vec{\rho}^{\mu\nu} + \frac{1}{2} m_\rho^2 \vec{\rho}_\mu \cdot \vec{\rho}^\mu, \quad (5)$$

with the usual definition of the ρ field strength tensor as

$$\vec{\rho}_{\mu\nu} = \partial_\mu \vec{\rho}_\nu - \partial_\nu \vec{\rho}_\mu. \quad (6)$$

Interactions between the π and ρ mesons are generated by minimally coupling derivative terms of the π and ρ fields to a ρ gauge field [36],

$$\begin{aligned} \partial_\mu &\rightarrow \partial_\mu + i g_\rho \vec{\rho}_\mu \cdot \vec{T} \\ \partial_\mu \pi^a &\rightarrow \partial_\mu \pi^a + g_\rho \epsilon_{abc} \rho_\mu^b \pi^c \\ \partial_\mu \rho_\nu^a &\rightarrow \partial_\mu \rho_\nu^a + g_\rho \epsilon_{abc} \rho_\mu^b \rho_\nu^c, \end{aligned} \quad (7)$$

where \vec{T} is the isospin-1 operator with components of $(T^a)_{bc} = -i\epsilon_{abc}$ [37] and g_ρ is the $\rho\pi\pi$ coupling constant. Introducing the above covariant derivatives into the free-field Lagrangian results in $\rho\pi\pi$ and $\rho\rho\rho$ interactions of

$$\mathcal{L}_{\rho\pi\pi} = -g_\rho \vec{\rho}^\mu \cdot (\partial_\mu \vec{\pi} \times \vec{\pi}), \quad (8)$$

$$\mathcal{L}_{\rho\rho\rho} = -\frac{1}{2} g_\rho \vec{\rho}^{\mu\nu} \cdot (\vec{\rho}_\mu \times \vec{\rho}_\nu). \quad (9)$$

Interactions with the isosinglet vector ω field are included via a Wess-Zumino term [29, 30],

$$\mathcal{L}_{WZ} = g_{\pi\rho\omega} \epsilon^{\mu\nu\alpha\beta} \partial_\alpha \omega_\beta \partial_\mu \vec{\rho}_\nu \cdot \vec{\pi}. \quad (10)$$

Applying the gauging procedure of Eq. (7) to the Wess-Zumino term generates a contact term

$$\mathcal{L}_{\rho\rho\pi\omega} = g_{\pi\rho\omega} g_\rho \epsilon^{\mu\nu\alpha\beta} \partial_\alpha \omega_\beta (\vec{\rho}_\mu \times \vec{\rho}_\nu) \cdot \vec{\pi}. \quad (11)$$

Interactions with photons are introduced through VMD. We neglect the coupling of the ω field to the electromagnetic current, as the $\omega\gamma$ coupling is suppressed by a factor of ≈ 3 –4 relative to the $\rho\gamma$ coupling [34]. Following Ref. [31], we parametrize the $\rho\gamma$ coupling with C_ρ ,

$$\mathcal{L}_{EM} = -A^\mu C_\rho m_\rho^2 \rho_\mu^0, \quad (12)$$

where A_μ is the photon field and ρ_μ^0 is the neutral ρ field.

For a realistic description of interaction processes, we also need to account for the finite size of the mesons, which we do in the standard way by introducing previously determined dipole hadronic form factors at each

vertex [31, 32]. For s -channel decay processes, we employ at each vertex the form

$$F(s) = \left(\frac{2\Lambda^2 + m_R^2}{2\Lambda^2 + [E_2(p_{CM}) + E_3(p_{CM})]^2} \right) \quad (13)$$

where $E_i(p_{CM}) = \sqrt{m_i^2 + p_{CM}^2}$ and $p_{CM}(s)$ is the center-of-mass momentum of each hadronic decay particle, $i=2,3$, Λ is an hadronic cut-off parameter (taken to be 1 GeV in the present work), and m_R is the mass of the resonant (or decay) particle. For t -channel scattering processes, we employ at each vertex the form

$$F(t) = \left(\frac{2\Lambda^2}{2\Lambda^2 + |t|} \right)^2, \quad (14)$$

with $t = (p_1 - p_3)^2$ for incoming (p_1) and outgoing (p_3) 4-momenta (and likewise for u -channel processes).

Save for s -channel decay processes or those processes with individually gauge-invariant vertices, the above implementation of form factors renders it a rather involved task to maintain gauge invariance, especially for scattering processes where multiple diagrams contribute [38]. Therefore, we follow the simplified prescription of Ref. [31] by introducing an overall factorized form factor squared for each scattering matrix element with an appropriately defined average momentum transfer. This is done by identifying the dominant diagram in the interaction process, i.e., the diagram with the largest contribution to the high-energy photo-emission rate of a given process (at low energies the form factor effects are small). Typically, this will be a t -channel exchange diagram with the lightest exchange particle (e.g., pion exchange in $\pi\rho \rightarrow \gamma\pi$), since s -channel processes are suppressed by propagators of the form $(s - m_R^2)^{-1}$. The average momentum transfer, \bar{t} , is evaluated from

$$\begin{aligned} & \left(\frac{1}{m_X^2 + |\bar{t}|} \right)^2 \left(\frac{2\Lambda^2}{2\Lambda^2 + |\bar{t}|} \right)^8 \\ &= -\frac{1}{4q_0^2} \int_0^{-4q_0^2} dt \left(\frac{1}{m_X^2 + |t|} \right)^2 \left(\frac{2\Lambda^2}{2\Lambda^2 + |t|} \right)^8, \quad (15) \end{aligned}$$

(and likewise if a u -channel process dominates), and is a function of only the photon energy and exchange-particle mass in the dominant diagram. This enables us to factorize the form factor from the total amplitude,

$$|\overline{\mathcal{M}}|^2 = |\overline{\mathcal{M}}_{\text{point}}|^2 F(\bar{t})^4, \quad (16)$$

and thus retain the gauge invariance in the amplitude, $\mathcal{M}_{\text{point}}$, which is evaluated for point-like vertices.

The coupling constants g_ρ and $g_{\pi\rho\omega}$ are evaluated using data from $\rho \rightarrow \pi\pi$ and $\omega \rightarrow \pi^0\gamma$ decays. In principle, the couplings C_ρ and g_ρ are related via VMD, such that $C_\rho = e/g_\rho$. However, for our Born diagrams, where we are using zero-width ρ mesons, we will instead use experimental data from the $\rho \rightarrow e^+e^-$ decay to evaluate C_ρ .

Using the s -channel form factor of Eq. (13), the decay rate becomes

$$\Gamma_{1 \rightarrow 2+3} = \frac{p_{CM} |\overline{\mathcal{M}}|^2 F^2(p_{CM})}{8\pi m_1^2}, \quad (17)$$

where m_1 is mass of the decaying particle and $|\overline{\mathcal{M}}|^2$ is the initial-state averaged and final-state summed matrix element of the associated decay process. Using Particle Data Group [39] values for $\Gamma_{\rho \rightarrow \pi\pi} = 149.1$ MeV, $\Gamma_{\omega \rightarrow \pi^0\gamma} = 0.703$ MeV, and $\Gamma_{\rho \rightarrow e^+e^-} = 7.04$ keV, and a form factor cutoff of $\Lambda = 1$ GeV, we find coupling constants of $g_\rho = 5.98$, $g_{\pi\rho\omega} = 21.6 \text{ GeV}^{-1*}$, and $C_\rho = 0.0611$.

Having established all necessary interaction vertices, including form factor effects and the quantitative evaluation of all coupling constants, we now proceed to the photo-emission rate calculations.

III. KINETIC THEORY

Within the framework of relativistic KT, thermal photon emission from the $\pi\rho\omega$ system with external ω particles arises from three $2 \rightarrow 2$ scattering processes: $\pi\rho \rightarrow \gamma\omega$, $\pi\omega \rightarrow \gamma\rho$, and $\rho\omega \rightarrow \gamma\pi$. Each of the three processes is composed of s -, t -, u -channel diagrams and a contact (c) term to ensure gauge invariance. The diagrams comprising each process in the $\pi\rho\omega$ system are shown in Fig. 1.

The evaluation of photo-emission rates using Eq. (4) requires the coherent sum of the four amplitudes of each diagram;

$$|\mathcal{M}|^2 = |\mathcal{M}_s + \mathcal{M}_t + \mathcal{M}_u + \mathcal{M}_c|^2. \quad (18)$$

We calculate the amplitudes by applying Feynman rules to the diagrams shown in Fig. 1 and using the Lagrangian interactions and form factor procedure detailed in Sec. II. The explicit expressions for the matrix elements are given in Appendix A.

Straightforward calculations of rates for the $\pi\rho\omega$ system using KT can be done for the $\pi\rho \rightarrow \gamma\omega$ and $\rho\omega \rightarrow \gamma\pi$ processes, while the $\pi\omega \rightarrow \gamma\rho$ process reveals a subtlety. In the u -channel diagram, Fig. 1(d), the exchanged pion can go on-shell, such that $u = (p_\omega - p_\gamma)^2 = m_\pi^2$. This induces a non-integrable singularity in the phase space of the rate calculation using Eq. (4). This pion pole configuration corresponds to the $\omega \rightarrow \pi^0\gamma$ radiative decay, which, in fact, has already been included in previous photo-emission calculations [31, 32]. Therefore we must eliminate this contribution from our results to avoid double-counting of the radiative ω decay. This is facilitated by the structure of the Wess-Zumino term,

* This slightly differs from the value of 25.8 GeV^{-1} in Ref. [32] since there the VMD value of $C_\rho = e/g = 0.052$ is used.

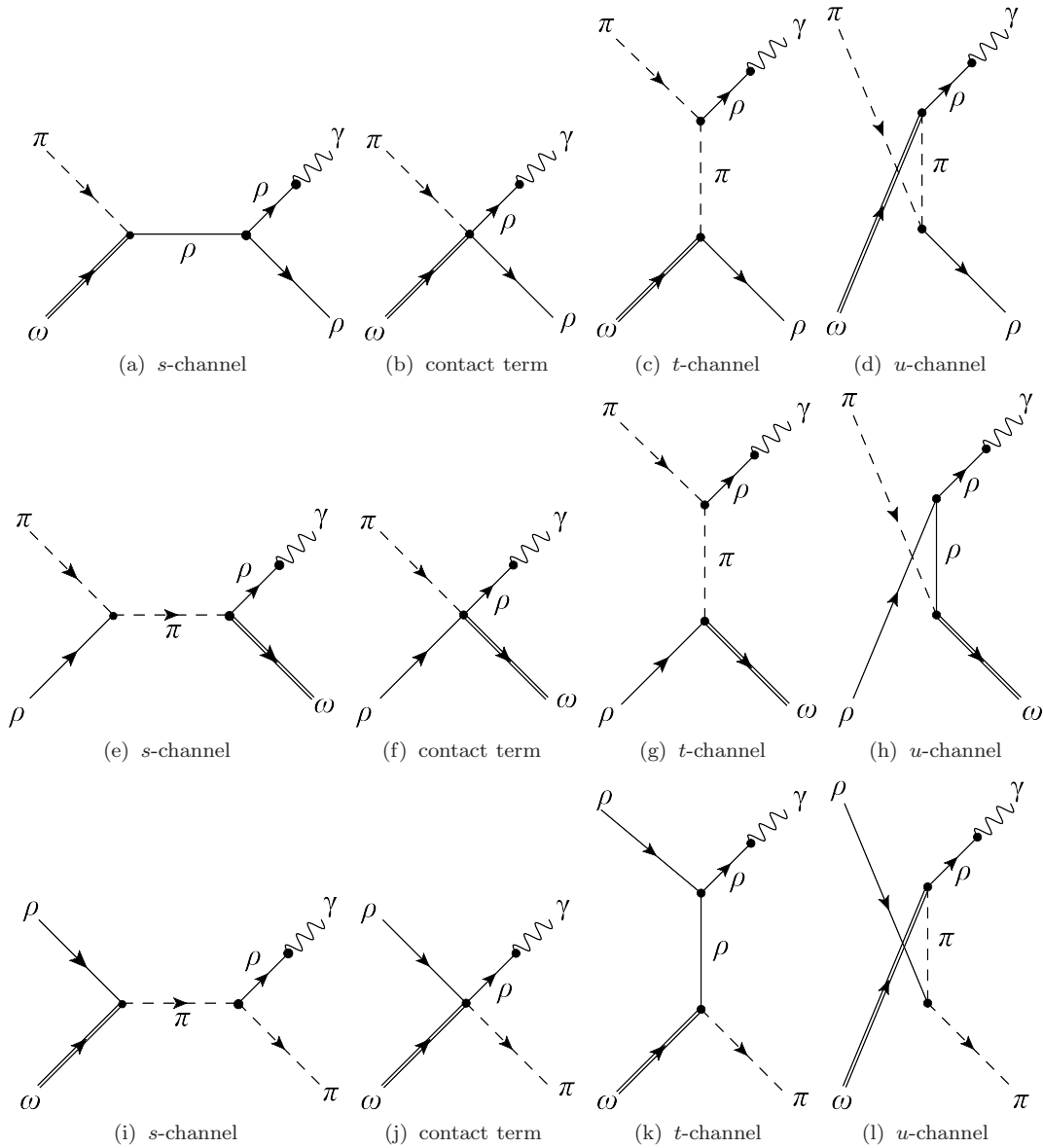


FIG. 1: Feynman Born diagrams for photon emission from the $\pi\rho\omega$ system, i.e., Figs. (a)-(d) for $\pi\omega \rightarrow \gamma\rho$, Figs. (e)-(h) for $\pi\rho \rightarrow \gamma\omega$, and Figs. (i)-(l) for $\rho\omega \rightarrow \gamma\pi$.

Eq. (10), which renders a diagram individually gauge-invariant when an outgoing ρ meson is converted to a photon. This feature allows us to separate the u -channel from the other three diagrams in the $\pi\omega \rightarrow \gamma\rho$ process while maintaining gauge invariance. Naïvely, we can avoid the ω decay by excluding timelike pion configurations with $u > 0$ from the integration range in Eq. (4), but *a priori* this is not a rigorous justification for this choice. To scrutinize this prescription to avoid double-counting of the ω decay, we turn to TFT where such an ambiguity does not occur.

IV. THERMAL FIELD THEORY

Thermal field theory provides a rigorous framework for the calculation of photo-emission rates. As discussed above, within the VMD model the relevant quantity is the ρ meson self-energy; recall Eqs. (1) and (2). Each process and channel considered in the KT calculation has a corresponding ρ self-energy diagram associated with it.

For our analysis, the relevant self-energy diagrams are depicted in Fig. 2, which encompass the u -channel diagrams of the $\rho\omega \rightarrow \gamma\pi$ and $\pi\omega \rightarrow \gamma\rho$ processes. The latter is the diagram which involves the divergence and double counting of the $\omega \rightarrow \pi^0\gamma$ decay, while the former will be considered to benchmark the equivalence between

the two methods. For both cases, we can separate the u -channel from the other channels and make a meaningful comparison because each diagram is gauge-invariant on its own due to the $\pi\rho\omega$ photo-emission vertex.

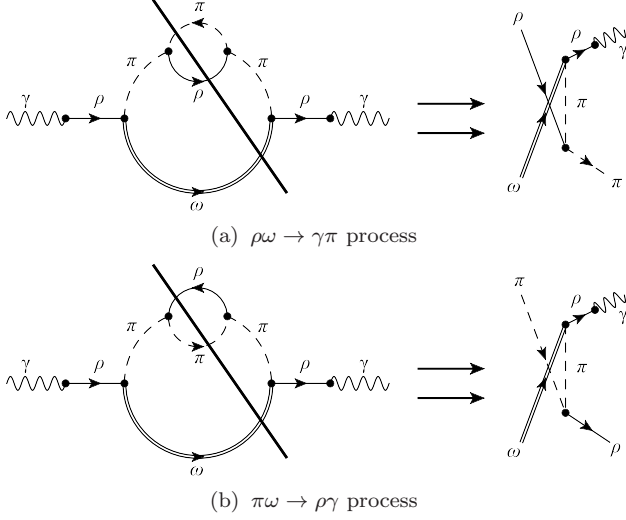


FIG. 2: Cuts of the photon self-energy which generate imaginary parts corresponding to the u -channel diagrams of the $\rho\omega \rightarrow \gamma\pi$ and $\pi\omega \rightarrow \gamma\rho$ processes.

The two diagrams in Fig. 2 have similar structures differing only by the implementation of the π self-energy in the inner loop. Using standard Feynman rules within the Matsubara formalism [40], the (transverse part of the) ρ self-energy encompassing both diagrams can be expressed as

$$\Sigma_{\rho}^T(q, T) = -\frac{1}{2} P_T^{\mu\mu'} g_{\pi\rho\omega}^2 \int \frac{d^3p}{(2\pi)^3} T \sum_{\omega_n} v_{\pi\rho\omega}^{\mu\nu} v_{\pi\rho\omega}^{\mu'\nu'} \times D_{\omega}^{\nu\nu'}(\omega_n, \vec{p}) D_{\pi}(q_0 - \omega_n, \vec{q} - \vec{p}), \quad (19)$$

where $v_{\pi\rho\omega}$ represents the $\pi\rho\omega$ vertex, \vec{p} is the three-momentum of the ω meson, and $D_{\omega, \pi}$ are the propagators of the ω and π mesons. When evaluating Σ_{ρ}^T at the photon point, the transverse projection operator, $P_T^{\mu\nu}$, can be replaced by the (negative) metric tensor $-g^{\mu\nu}$, as they are equivalent for a gauge invariant self-energy.

We will focus on calculating the imaginary part of the ρ self-energy, since the real part is small compared to the ρ mass and thereby does not significantly contribute to the rates. First, each propagator is expressed in terms of a dispersion relation;

$$D(p_0, \vec{p}) = -\frac{1}{\pi} \int_{-\infty}^{\infty} d\omega \frac{\text{Im} D(\omega, \vec{p})}{p_0 - \omega + i\epsilon}. \quad (20)$$

The ω is considered a zero-width particle corresponding to being an external particle in the KT calculation. Using

$$\text{Im} D_{\omega}(p_0, \vec{p}) = -\pi \delta(p_0^2 - \vec{p}^2 - m_{\omega}^2), \quad (21)$$

evaluating the Matsubara sum in Eq. (19), and taking

the ρ self-energy to the photon point, $q_0 = |\vec{q}|$, yields

$$\begin{aligned} \text{Im} \Sigma_{\rho}(q_0, \vec{q}, T) &= g_{\pi\rho\omega}^2 \int \frac{d^3p}{(2\pi)^3} \frac{1}{2E_{\omega}} \\ &\times \left\{ (E_{\omega} q_0 - \vec{p} \cdot \vec{q})^2 \text{Im} D_{\pi}(q_0 - E_{\omega}, \vec{q} - \vec{p}) \right. \\ &\quad [1 + f^{\pi}(q_0 - E_{\omega}, T) + f^{\omega}(E_{\omega}, T)] \\ &\quad - (E_{\omega} q_0 + \vec{p} \cdot \vec{q})^2 \text{Im} D_{\pi}(E_{\omega} - q_0, \vec{q} - \vec{p}) \\ &\quad \left. [f^{\pi}(E_{\omega} - q_0, T) - f^{\omega}(E_{\omega}, T)] \right\}, \quad (22) \end{aligned}$$

where $E_{\omega} = \sqrt{\vec{p}^2 + m_{\omega}^2}$.

The inner loop constitutes a pion self-energy which figures in the pion propagators of Eq. (22). For interactions with thermal mesons, m , this pion self-energy has the form [32]

$$\Sigma_{\pi m}(k_0, \vec{k}, T) = \int \frac{d^3p}{(2\pi)^3} \frac{\mathcal{M}_{\pi m}(p, k_0, \vec{k})}{2E_m} \times \left\{ f^m(E_m, T) - f^{\pi m}(E_m + k_0, T) \right\}, \quad (23)$$

where $\mathcal{M}_{\pi m}$ is the pertinent forward scattering amplitude. Here we consider thermal mesons $m = \pi, \rho$, with either $\pi\pi$ scattering through an s -channel ρ resonance, or $\pi\rho$ scattering through an s -channel π resonance. As indicated by the arrows in the diagrams of Fig. 2, taking the imaginary part of each ρ self-energy yields the corresponding u -channel Born diagram. The π self-energy $\Sigma_{\pi\pi}$ generates the $\rho\omega \rightarrow \gamma\pi$ process, and the π self-energy $\Sigma_{\pi\rho}$ generates the $\pi\omega \rightarrow \gamma\rho$ process.

In the following two subsections we will analyze these two processes in more detail. In Sec. IV A, we use the $\rho\omega \rightarrow \gamma\pi$ process as a benchmark to establish the equivalence of the photo-emission rates calculated using TFT to 2-loop order with KT using Born amplitudes. In Sec. IV B, we then use the TFT calculation to identify a selection criterion that allows us to eliminate double-counting with the ω radiative decay.

A. $\rho\omega \rightarrow \gamma\pi$ u -channel

While the u -channel diagram of the $\rho\omega \rightarrow \gamma\pi$ process is structurally similar to that of $\pi\omega \rightarrow \gamma\rho$ process, the key difference is that in the former the exchanged π cannot go on shell. This enables straightforward calculations for this process using both KT and TFT. The pertinent imaginary part of the ρ self-energy has two major contributions indicated by the two terms in braces in Eq. (22) and schematically shown in Fig. 3. These two contributions, commonly referred to as the Landau and unitarity cuts (representing $\rho\pi \rightarrow \omega$ scattering and $\rho \rightarrow \pi\omega$ decay processes for the left-hand-side vertex), can be interpreted based on the direction of energy flow of the virtual pion. For the right-hand-side vertex, the unitarity cut is associated with a pion energy flow oriented into the

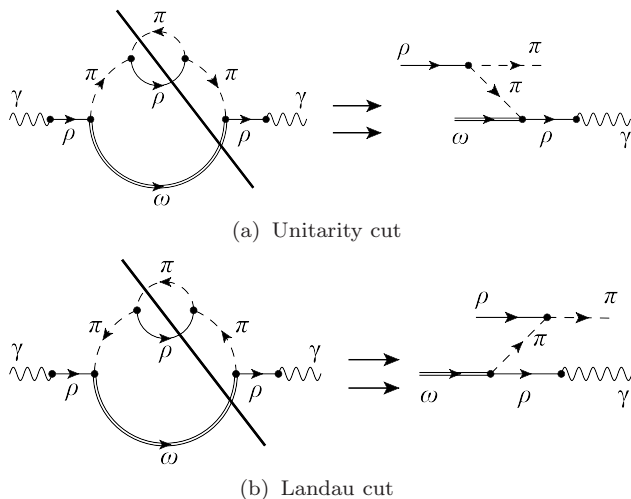


FIG. 3: Two cuts of the photon self-energy which give rise to imaginary parts corresponding to the u -channel diagram of the $\rho\omega \rightarrow \gamma\pi$ process.

$\pi\rho\omega$ vertex, as shown in Fig. 3(a), and is associated with $E_\omega < q_0$. This cut corresponds to first term of Eq. (22). The Landau cut is associated with a pion energy flow oriented out of the $\pi\rho\omega$ vertex, shown in Fig. 3(b), and corresponds to the second term of Eq. (22), or $E_\omega > q_0$.

We have calculated the pertinent imaginary parts of the ρ self-energy given by Fig. 3 and inserted them into Eq. (1)[†] to obtain the corresponding photo-emission rates; the results for a temperature of $T = 150$ MeV are shown in Fig. 4 and compared to the KT calculation (both without form factors). We find very good agreement between the sum of the Landau and unitarity cuts in TFT and the KT Born amplitude calculation, thus confirming the equivalence of the two methods. In addition, we have verified that the Landau (unitarity) cut contribution in the TFT calculation can be directly mapped to a calculation in KT where the phase space integral is restricted to the energy of the exchanged pion flowing out of (in to) the $\pi\rho\omega$ vertex ($E_\omega >$ or $< q_0$, respectively). The identification of the mapping between Landau and unitarity cuts and KT for this process ($\rho\omega \rightarrow \gamma\pi$) is facilitated by the fact that the u -channel Born diagram does not develop any on-shell singularities (contrary to the $\pi\omega \rightarrow \gamma\rho$ process discussed below).

Figure 3(b) shows that the Landau cut gives rise to a Born diagram featuring a $\omega \rightarrow \pi\gamma$ radiative decay topology. However, the emitted π is necessarily spacelike as it is absorbed by an on-shell ρ turning into an on-shell pion. Likewise, in the Born diagram generated from the unitarity cut an on-shell ω absorbs a π turning into a massless photon, requiring a spacelike π . Similar consid-

[†] As in the KT calculations, we use C_ρ as the EM $\rho\gamma$ coupling in Eq. (1) instead of the VMD value of e/g .

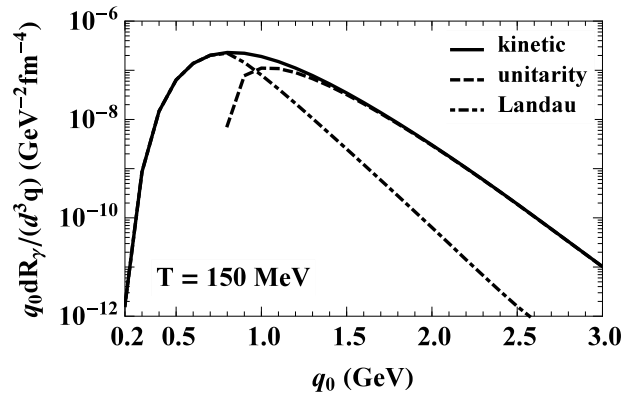


FIG. 4: Results from photo-emission calculation of $\rho\omega \rightarrow \gamma\pi$ via the u -channel diagram at $T = 150$ MeV. The solid line is the result using KT over the full kinematic range of the exchanged pion, the dashed line is from TFT via the unitarity cut of Fig. 3, and the dot-dashed is from the Landau cut of Fig. 3. The sum of the unitarity and Landau cuts is plotted but cannot be seen as it coincides with the solid curve.

erations for the unitarity and Landau cuts will be used in the following section to separate out on-shell ω decays in the $\pi\omega \rightarrow \gamma\rho$ process.

The TFT calculation affords us with yet another benefit, namely to evaluate the effects of a finite width on the ρ mesons which appear as external particles in the Born calculations within kinetic theory. This effect has been studied previously within the latter framework and found to be negligible [41]. Within TFT we can render this check more rigorous by including a finite width for the ρ meson in the integral for the $\pi\rho$ loop in Fig. 3(a). We found variations of order 10% or less of the photo-emission rates, corroborating the results of Ref. [41].

B. $\pi\omega \rightarrow \gamma\rho$ u -channel

We now utilize TFT to calculate the photo-emission rate given by the ρ self-energy in Fig. 2(b) where the inner loop is a pion self-energy induced by an interaction with a thermal ρ meson forming a π , i.e., $\Sigma_{\pi\rho}$ from Eq. (23). Unlike its KT counterpart, this calculation is well defined, without any divergences associated with, e.g., a pion pole.

Again, as illustrated in Fig. 5, the ρ self-energy can be separated into unitarity and Landau cuts. However, in this process the exchanged π in the Landau cut can go on-shell. When this occurs the Landau cut corresponds to the radiative ω decay of $\omega \rightarrow \pi^0\gamma$. This contribution has already been included in previous calculations of thermal photo-emission rates [32], and does not constitute a new hadronic source from the $\pi\rho\omega$ system.

We now use the distinction between the Landau and unitarity cuts provided by TFT as a selection criterion for what to include in our rates. We will drop the contri-

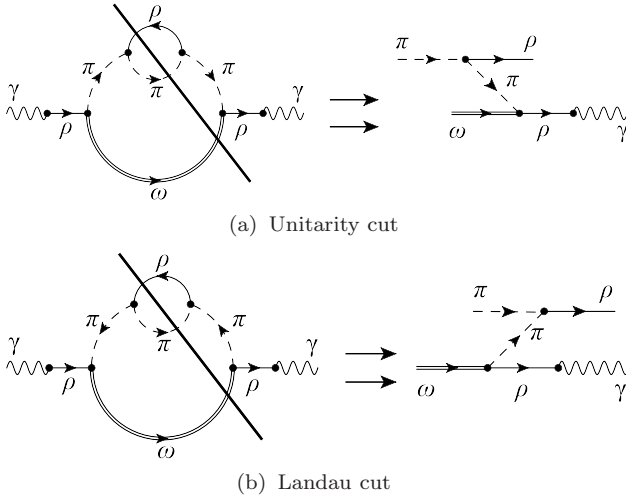


FIG. 5: Two cuts of the photon self-energy which give rise to imaginary parts corresponding to the u -channel diagram of the $\pi\omega \rightarrow \gamma\rho$ process.

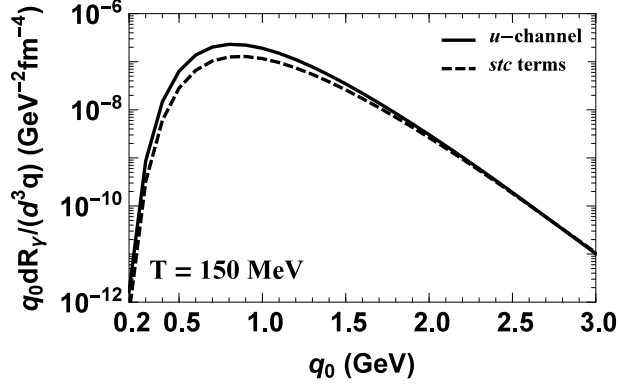


FIG. 6: Comparison of the contributions to the $\rho\omega \rightarrow \gamma\pi$ process from the u -channel diagram (solid line) and the combined stc terms (dashed line); no form factors included.

tribution from the Landau cut altogether, corresponding to the exchange of timelike pions, to preclude any double-counting with the radiative ω decay. The remaining contribution from the unitarity cut calculated with TFT is found to agree with KT when the integration over phase space is restricted to pion energies such that $q_0 > E_\omega$. In principle, this is a conservative choice since it excludes not only all timelike pions but also spacelike ones with positive energy. In practice, this difference appears to be negligible.

V. THERMAL PHOTON RATES FROM $\pi\rho\omega$ INTERACTIONS

Before coming to our final results, let us briefly elaborate on the concrete implementation of form factors for the processes at hand. The $\pi\omega \rightarrow \gamma\rho$ process is dom-

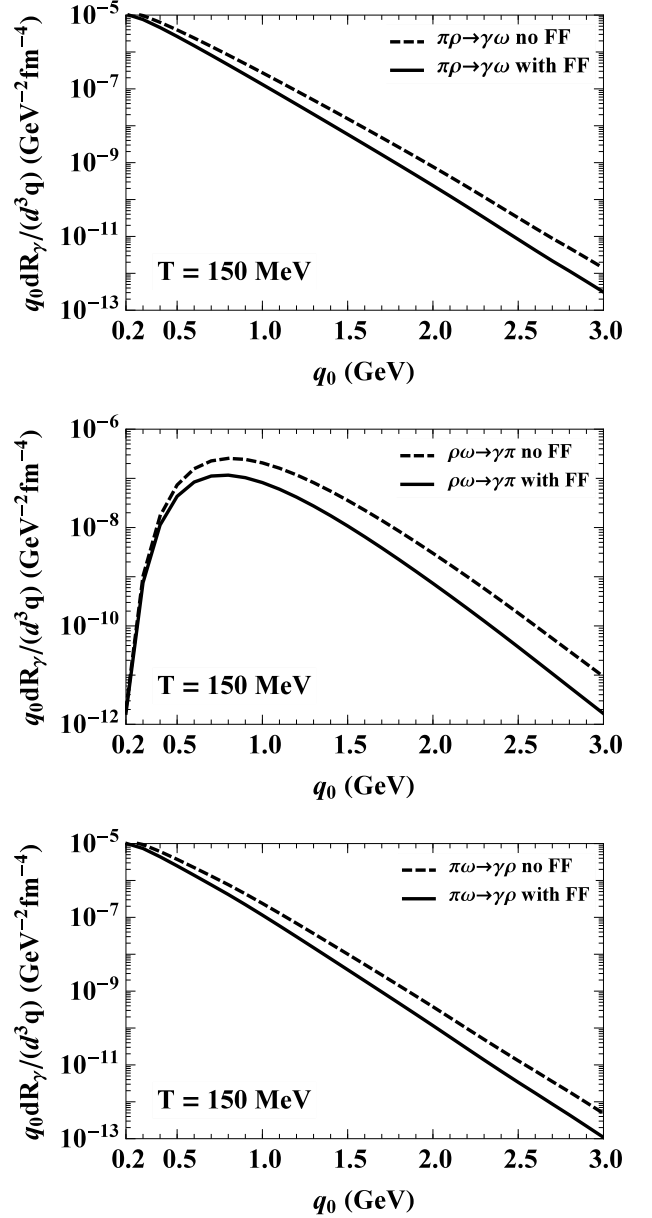


FIG. 7: Impact of hadronic form factors on the photo-emission rates at $T = 150 \text{ MeV}$ for $\pi\rho \rightarrow \gamma\omega$ (upper panel), $\rho\omega \rightarrow \gamma\pi$ (middle panel), and $\pi\omega \rightarrow \gamma\rho$ (lower panel) processes. The rates with form factor (solid lines) are compared to the ones without form factor (dashed lines).

inated by the t - and u -channel pion exchanges. Since the t - and u -channel form factors have the same structure, their factorized average form factor is identical and is thus applied as overall form factor to all diagrams in this process. In the $\pi\rho \rightarrow \gamma\omega$ system, the pion t -channel exchange is expected to prevail over the u -channel, which is suppressed by the ρ mass in the propagator. Therefore the pertinent factorized average t -channel form factor is employed. Before implementation of form factors, the $\rho\omega \rightarrow \gamma\pi$ process has two approximately equal con-

tributions: the u -channel and the combined contact, s -, and t -channel terms (“ stc ” for brevity), cf. Fig. 6. Note that both u and the stc diagrams are individually gauge invariant which affords us the possibility to treat these two contributions separately. As discussed in Sec. II, the suppression generated by the averaged factorized form factors is driven by the mass of the exchanged particle. The u -channel diagram involves an exchanged π whose associated form factor generates a suppression of up to a factor 4.5 at $q_0 = 3.0$ GeV. On the other hand, the stc term is dominated by t -channel ρ exchange at high energies, whose associated average form factor generates a suppression of up to a factor 30 at $q_0 = 3.0$ GeV. Clearly, the choice of either from factor would not be an accurate procedure. However, due to the separate gauge invariance of the u and stc terms, we can apply an average π exchange form factor (F_π) to the u -channel, an average ρ exchange form factor (F_ρ) to the stc term, and a combination of the two form factors to the interference term (which is also gauge invariant), schematically given by

$$|\mathcal{M}_{\text{FF}}|^2 = F_\pi^4 |\mathcal{M}_u|^2 + F_\rho^4 |\mathcal{M}_{stc}|^2 + F_\pi^2 F_\rho^2 (\mathcal{M}_u \mathcal{M}_{stc}^* + \mathcal{M}_{stc} \mathcal{M}_u^*) . \quad (24)$$

The net effect of this implementation for the $\rho\omega \rightarrow \gamma\pi$ process is that the total rate is suppressed by a somewhat larger magnitude than the other two processes, but still less suppressed than if we had used an overall t -channel ρ -exchange form factor. The quantitative effects of the form factors are illustrated in Fig. 7 for each of the three processes at a temperature of $T = 150$ MeV.

One may wonder how variations in the form factor cutoff affect the emission rates. The cutoff parameter of $\Lambda_{\pi\rho\omega} = 1$ GeV (as used throughout this work) has been fixed together with the $\pi\rho\omega$ coupling constant in Ref. [32], to reproduce the radiative and hadronic ω decays. However, a somewhat smaller cutoff, say, $\Lambda_{\pi\rho\omega} = 0.8$ GeV, still gives agreement with those data once the coupling constant is increased accordingly. We have verified that using the latter set of parameters leads to an insignificant change of our photon emission rates over the relevant range of photon energies of up to ≈ 5 GeV.

Our final photo-emission rates for the three processes from the $\pi\rho\omega$ system (including form factors) are summarized in Fig. 8 for three different temperatures of 120, 150, and 180 MeV. In the phenomenologically important regime of photon energies around ≈ 1 GeV all three channels are of comparable magnitude. The $\rho\omega \rightarrow \gamma\pi$ channel falls off significantly below that, but becomes the dominant photon source at energies above 1.2-1.5 GeV for all temperatures. The relative spectral strengths of the three channels are rather stable with temperature; only the $\pi\rho \rightarrow \gamma\omega$ rate increases slightly relative to the other two at higher energies. We provide parametrizations of the final rates in Appendix B. While the applicability of the present methods of thermal photon calculations is questionable at temperatures close to the pseudo-critical transition temperature, we include parametrizations up

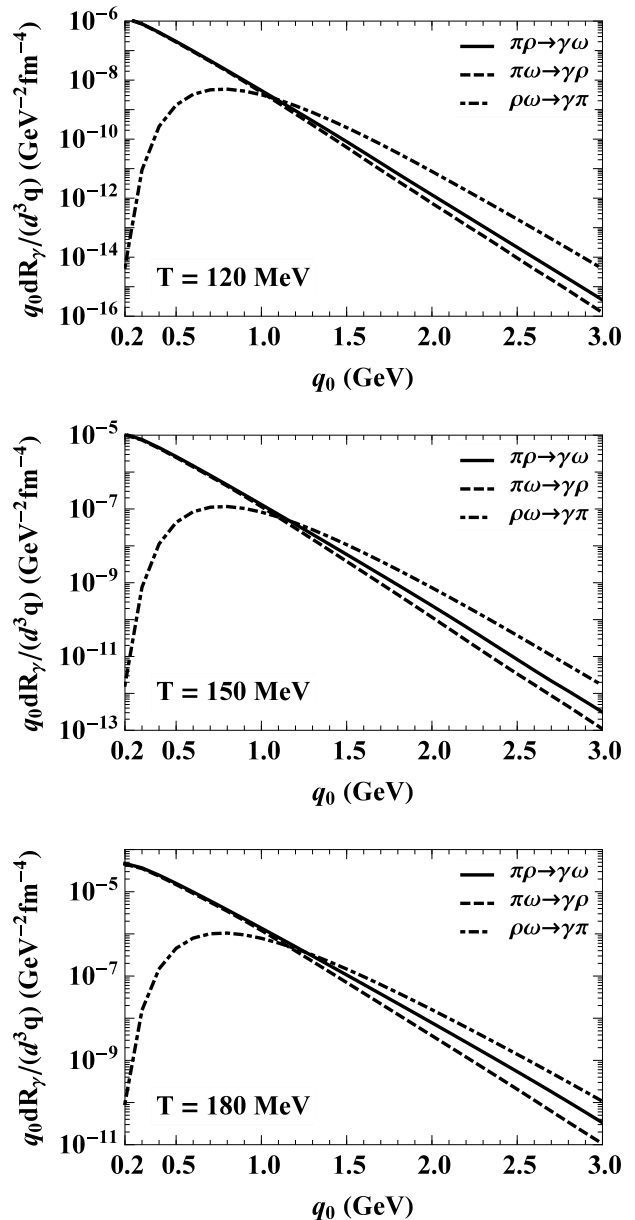


FIG. 8: Thermal photo-emission rates from the $\pi\rho\omega$ system for $\pi\rho \rightarrow \gamma\omega$ (solid lines), $\pi\omega \rightarrow \gamma\rho$ (dashed lines), and $\rho\omega \rightarrow \gamma\pi$ (dot-dashed lines) for temperatures $T = 120, 150$ and 180 MeV (upper, middle and lower panel, respectively). Form factor effects are included.

to $T = 180$ MeV for usage in a variety of thermal evolution models which may have the phase transition implemented at different temperatures.

At last, we compare the total rate from the newly calculated processes with existing literature, specifically, the ω t -channel exchange in $\pi\rho \rightarrow \gamma\pi$ as calculated in Ref. [31] (Fig. 9) and $\pi\pi$ Bremsstrahlung from Refs. [42, 43] (Fig. 10). The former process involves the same vertices as considered in the present work but with the ω as an exchange particle rather than an external one;

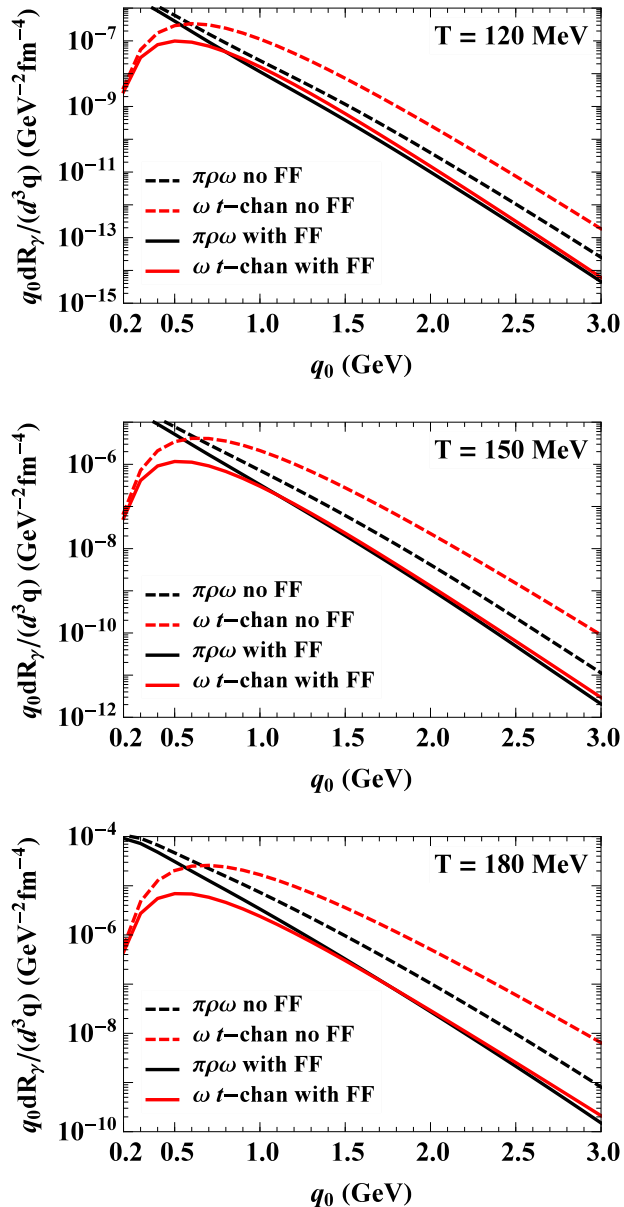


FIG. 9: Total rates from the $\pi\rho$ system as calculated in the present work (black lines) versus the ω t -channel rate (red line) for temperatures $T = 120, 150$ and 180 MeV (upper, middle and lower panel, respectively). Dashed lines are without form factor; solid lines are with form factor.

the pertinent rate was found to be a significant source of thermal photons for energies $q_0 \geq 1.5$ GeV relative to other known sources in hot and dense hadronic matter [31, 43]. Prior to the inclusion of form factors, the sum of the newly calculated rates is smaller than the ω t -channel exchange in the $\pi\rho \rightarrow \gamma\pi$ process by a factor of ca. 4-8 for $q_0 > 1$ GeV. In the realistic case with form factors, however, the two rates are rather close in the phenomenologically most relevant range of $q_0 < 2$ GeV. In practice, in URHICs at RHIC and LHC energies, this

approximately translates into lab-momenta of $q_t < 4$ GeV due to blue-shift effects of the exploding fireball [44]. In Refs. [42, 43], $\pi\pi$ Bremsstrahlung was found to be appreciable for photon energies of less than 1 GeV, even exceeding the contribution from in-medium ρ mesons with baryonic sources [45, 46] at the lowest photon energies. Fig. 10 shows that the rates from the $\pi\rho$ system are comparable to the Bremsstrahlung rates for photon energies between 0.5 and 1 GeV, which suggests that the contribution of this new photon source is significant relative to existing thermal photon rate calculations.

In addition, below the chemical freezeout temperature of $T_{\text{ch}} \simeq 160$ in URHICs, effective meson chemical potentials build up, in particular for pions, which further augment two of the three newly calculated rates. The $\pi\omega \rightarrow \gamma\rho$ and $\rho\omega \rightarrow \gamma\pi$ processes will pick up pion fugacity factors $z_\pi = \exp(\mu_\pi/T)$ to the 4th and 5th powers, respectively, compared to the 3rd power for $\pi\rho \rightarrow \gamma\pi$ processes. With this enhancement from pion fugacities, the thermal photon emission processes calculated could provide a non-negligible contribution to the direct-photon spectra in URHICs [26].

In our current study, we have focused on the $\pi\rho\omega$ system due to its known large coupling constant and the relatively small masses of these hadrons. Decay contributions of higher resonances as intermediate particles in hadron- ρ scattering processes have been considered in Ref. [32] and found to give subleading contributions at the photon point (cf. Fig. 1 in that reference). The question remains whether the scattering of higher-mass states can give significant contributions. As an example, let us consider the a_1 as an external particle. This is the next higher-mass particle with a known large coupling to $\pi\rho$ and $\pi\gamma$, and closely resembles the $\pi\rho\omega$ system in the pertinent photon-emitting processes. Inspection of Fig. 1 of Ref. [32] reveals that the a_1 contribution to the ρ self-energy is down by about an order of magnitude compared to the ω at the photon point. This factor can be readily

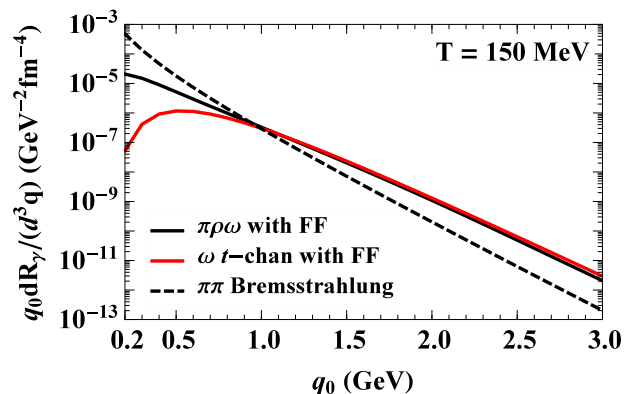


FIG. 10: Total rates at $T = 150$ MeV from the $\pi\rho\omega$ system (solid black line) compared to the $\pi\pi$ Bremsstrahlung rate (dashed black line) [42, 43] and the $\pi\rho \rightarrow \gamma\pi\omega$ t -channel rate (red line).

understood by realizing that the $\pi\rho\omega$ coupling is a factor 2 larger than the $\pi\rho a_1$ coupling, and that the thermal a_1 density is suppressed by more than a factor of 3 at temperatures of $T = 150$ MeV.

VI. CONCLUSIONS

In this work, we have calculated the photo-emission rates from the tree-level scattering processes $\pi\rho \rightarrow \gamma\omega$, $\pi\omega \rightarrow \gamma\rho$, and $\rho\omega \rightarrow \gamma\pi$ using relativistic kinetic theory. Complementary calculations were performed using thermal field theory for the u -channel diagrams of two of the processes. This allowed us to (a) explicitly establish consistency between the two methods (as well as exert quality control of the results) and (b) identify a criterion by which to exclude singular contributions from the exchange of on-shell pions in $\pi\omega \rightarrow \gamma\rho$ and thus avoid double-counting with the ω radiative decay. After the inclusion of hadronic vertex form factors, which suppress

the rates at high energies, our total rate resulting from all three processes turns out to be comparable to the ω t -channel rates in the $\pi\rho \rightarrow \gamma\pi$ process [31] and to $\pi\pi$ Bremsstrahlung [42]. Our results thus provide an enhancement of existing rate calculations in the direction of what has been conjectured in Ref. [26]; we anticipate that thermal emission from $\pi\rho\omega$ interactions will give a sizable contribution to direct-photon spectra in heavy-ion collisions. The precise extent to which the new thermal photon sources may help to reduce discrepancies with experimental spectra and elliptic flow will require their implementation into evolution models for the fireball in heavy-ion collisions. Work in this direction is in progress.

Acknowledgments

This work is supported by the US National Science Foundation under grant no. PHY-1306359.

Appendix A: Born Matrix Elements

In this appendix, we write out the matrix elements corresponding to each Feynman diagram in the $\pi\rho\omega$ system, explicitly indicating isospin indices and labeling each particle's four-momentum. They are derived by applying standard Feynman rules to the diagrams shown in Fig. 1 and using the interaction Lagrangians of Eqs. (8)-(12).

- $\pi^a(p_1) \rho^b(p_2) \rightarrow \gamma(q) \omega(p_3)$ process with isospin indices $\pi^a \rho^b$:

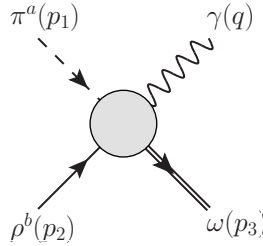


FIG. 11: Diagram showing four-momenta labels and isospin indices for the process $\pi\rho \rightarrow \gamma\omega$.

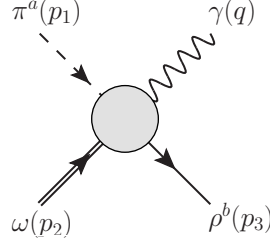
$$\mathcal{M}_s = -\frac{g_{\pi\rho\omega}g_\rho C_\rho}{s - m_\pi^2} (2p_1 - p_2)_\delta q^\mu q^\alpha \epsilon_{\mu\gamma\alpha\beta} \epsilon^\delta(p_2) \epsilon^{*\gamma}(q) \epsilon^{*\beta}(p_3) \epsilon^{3ab} \quad (\text{A1})$$

$$\mathcal{M}_t = -\frac{g_{\pi\rho\omega}g_\rho C_\rho}{t - m_\pi^2} (2p_1 - q)_\gamma p_2^\mu q^\alpha \epsilon_{\mu\delta\alpha\beta} \epsilon^\delta(p_2) \epsilon^{*\gamma}(q) \epsilon^{*\beta}(p_3) \epsilon^{3ab} \quad (\text{A2})$$

$$\mathcal{M}_u = -\frac{g_{\pi\rho\omega}g_\rho C_\rho}{t - m_\rho^2} (p_2 - q)^\mu q^\alpha \left(-g^{\nu\lambda} + \frac{(p_2 - q)^\nu (p_2 - q)^\lambda}{m_\rho^2} \right) \quad (\text{A3})$$

$$\begin{aligned} & [-g_{\delta\gamma}(p_2 + q)_\lambda - g_{\gamma\lambda}(p_2 - 2q)^\delta + g_{\delta\lambda}(2p_2 - q)_\gamma] \epsilon_{\mu\nu\alpha\beta} \epsilon^\delta(p_2) \epsilon^{*\gamma}(q) \epsilon^{*\beta}(p_3) \epsilon^{3ab} \\ \mathcal{M}_c = & -g_{\pi\rho\omega}g_\rho C_\rho q^\alpha \epsilon_{\gamma\delta\alpha\beta} \epsilon^\delta(p_2) \epsilon^{*\gamma}(q) \epsilon^{*\beta}(p_3) \epsilon^{3ab} \quad (\text{A4}) \end{aligned}$$

- $\pi^a(p_1) \omega(p_2) \rightarrow \gamma(q) \rho^b(p_3)$ process with isospin indices $\pi^a \rho^b$:

FIG. 12: Diagram showing four-momenta labels and isospin indices for the process $\pi\omega \rightarrow \gamma\rho$.

$$\mathcal{M}_s = -\frac{g_{\pi\rho\omega}g_\rho C_\rho}{s - m_\rho^2} p_1^\mu p_2^\alpha \left(-g^{\nu\lambda} + \frac{(q + p_3)^\nu (q + p_3)^\lambda}{m_\rho^2} \right) \quad (\text{A5})$$

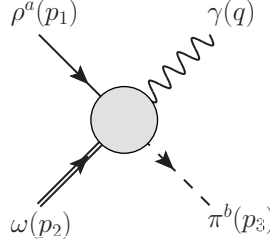
$$[g_{\lambda\delta}(q + 2p_3)_\gamma - g_{\lambda\gamma}(2q + p_3)_\delta + g_{\gamma\delta}(q - p_3)_\lambda] \epsilon_{\mu\nu\alpha\beta} \epsilon^\beta(p_2) \epsilon^{*\gamma}(q) \epsilon^{*\delta}(p_3) \epsilon^{3ab} \quad (\text{A6})$$

$$\mathcal{M}_t = \frac{g_{\pi\rho\omega}g_\rho C_\rho}{t - m_\pi^2} (p_1 - q)^\mu p_2^\alpha (2p_1 - q)_\gamma \epsilon_{\mu\delta\alpha\beta} \epsilon^\beta(p_2) \epsilon^{*\gamma}(q) \epsilon^{*\delta}(p_3) \epsilon^{3ab} \quad (\text{A7})$$

$$\mathcal{M}_u = \frac{g_{\pi\rho\omega}g_\rho C_\rho}{u - m_\pi^2} (p_2 - q)^\mu p_2^\alpha (p_1 - p_2 + q)_\delta \epsilon_{\mu\gamma\alpha\beta} \epsilon^\beta(p_2) \epsilon^{*\gamma}(q) \epsilon^{*\delta}(p_3) \epsilon^{3ab} \quad (\text{A8})$$

$$\mathcal{M}_c = g_{\pi\rho\omega}g_\rho C_\rho p_2^\alpha \epsilon_{\delta\gamma\alpha\beta} \epsilon^\beta(p_2) \epsilon^{*\gamma}(q) \epsilon^{*\delta}(p_3) \epsilon^{3ab} \quad (\text{A8})$$

- $\rho^a(p_1) \omega(p_2) \rightarrow \gamma(q) \pi^b(p_3)$ process with isospin indices $\rho^a \pi^b$:

FIG. 13: Diagram showing four-momenta labels and isospin indices for the process $\rho\omega \rightarrow \gamma\pi$.

$$\mathcal{M}_s = \frac{g_{\pi\rho\omega}g_\rho C_\rho}{s - m_\pi^2} p_1^\mu p_2^\alpha (q + 2p_3)_\gamma \epsilon_{\mu\delta\alpha\beta} \epsilon^\delta(p_1) \epsilon^\beta(p_2) \epsilon^{*\gamma}(q) \epsilon^{3ab} \quad (\text{A9})$$

$$\mathcal{M}_t = -\frac{g_{\pi\rho\omega}g_\rho C_\rho}{t - m_\rho^2} (p_1 - q)^\mu p_2^\alpha \left(-g^{\nu\lambda} + \frac{(p_1 - q)^\nu (p_1 - q)^\lambda}{m_\rho^2} \right) \quad (\text{A10})$$

$$[-g_{\delta\gamma}(p_1 + q)_\lambda - g_{\gamma\lambda}(p_1 - 2q)_\delta + g_{\delta\lambda}(2p_1 - q)_\gamma] \epsilon_{\mu\nu\alpha\beta} \epsilon^\delta(p_1) \epsilon^\beta(p_2) \epsilon^{*\gamma}(q) \epsilon^{3ab}$$

$$\mathcal{M}_u = \frac{g_{\pi\rho\omega}g_\rho C_\rho}{u - m_\pi^2} p_3^\mu p_2^\alpha (p_2 - q + p_3)_\delta \epsilon_{\mu\gamma\alpha\beta} \epsilon^\delta(p_1) \epsilon^\beta(p_2) \epsilon^{*\gamma}(q) \epsilon^{3ab} \quad (\text{A11})$$

$$\mathcal{M}_c = g_{\pi\rho\omega}g_\rho C_\rho p_2^\alpha \epsilon_{\delta\gamma\alpha\beta} \epsilon^\delta(p_1) \epsilon^\beta(p_2) \epsilon^{*\gamma}(q) \epsilon^{3ab} \quad (\text{A12})$$

Appendix B: Parametrizations

In this appendix, we present parametrizations of the photo-emission rates for each process in the $\pi\rho\omega$ system, along with plots of comparisons of parametrizations to calculated rates. We have verified the accuracy of the parametrizations to within 10% for temperature and photon energy ranges of $100 \text{ MeV} \leq T \leq 180 \text{ MeV}$ and $0.2 \text{ GeV} \leq q_0 \leq 5.0 \text{ GeV}$, except for the lowest photon energies of the $\rho\omega \rightarrow \gamma\pi$ process, whose overall contribution in that photon energy range is negligible. Form factor effects are included in all rate parametrizations.

• $\pi\rho \rightarrow \gamma\omega$

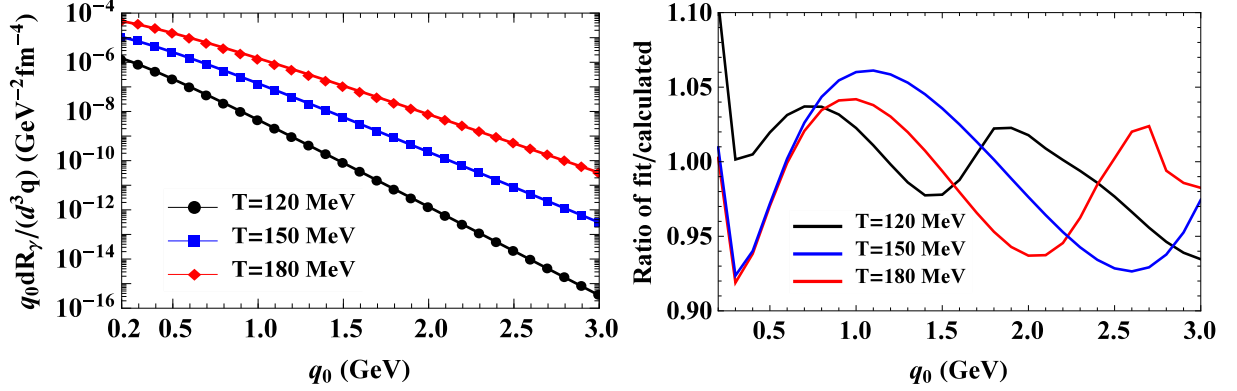


FIG. 14: Left panel: Calculated thermal photo-emission rates from the $\pi\rho \rightarrow \gamma\omega$ process (symbols) compared to the parametrized rates (lines). Right panel: Ratio of parametrized rates to calculated rates.

$$q_0 \frac{dR_{\pi\rho \rightarrow \gamma\omega}}{d^3 q} = \exp [a_1 q_0 + a_2 + a_3 q_0^{a_4} + a_5 (q_0 + a_6)^{a_7}] [\text{fm}^{-4} \text{GeV}^{-2}] , \quad (\text{B1})$$

$$\begin{aligned} a_1(T) &= -35.8991 + 460.425 T - 2592.04 T^2 + 5342.32 T^3 , \\ a_2(T) &= -41.9725 + 601.952 T - 3587.8 T^2 + 7604.97 T^3 , \\ a_3(T) &= 0.740436 - 16.7159 T + 133.526 T^2 - 347.589 T^3 , \\ a_4(T) &= 2.00611 - 3.79343 T + 29.3101 T^2 - 72.8725 T^3 , \\ a_5(T) &= -8.33046 + 121.091 T - 801.676 T^2 + 1712.16 T^3 , \\ a_6(T) &= 17.9029 - 388.5 T + 2779.03 T^2 - 6448.4 T^3 , \\ a_7(T) &= -15.622 + 340.651 T - 2483.18 T^2 + 5870.61 T^3 . \end{aligned} \quad (\text{B2})$$

• $\pi\omega \rightarrow \gamma\rho$

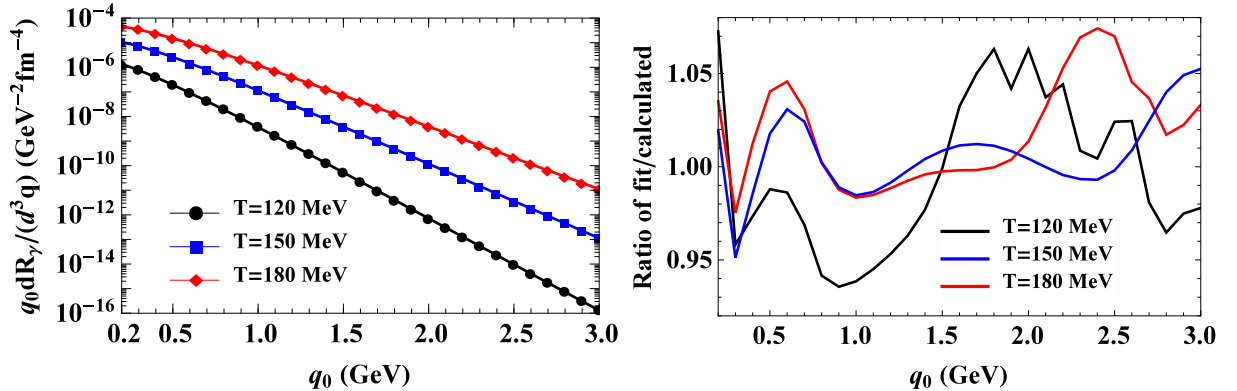


FIG. 15: Left panel: Calculated thermal photo-emission rates from the $\pi\omega \rightarrow \gamma\rho$ process (symbols) compared to the parametrized rates (lines). Right panel: Ratio of parametrized rates to calculated rates.

$$q_0 \frac{dR_{\pi\omega \rightarrow \gamma\rho}}{d^3q} = \exp [a_1 q_0 + a_2 + a_3 q_0^{a_4} + a_5 (q_0 + a_6)^{a_7}] [\text{fm}^{-4} \text{GeV}^{-2}] , \quad (\text{B3})$$

$$\begin{aligned}
a_1(T) &= -29.4663 + 291.356 T - 1301.27 T^2 + 2102.12 T^3 , \\
a_2(T) &= -45.081 + 688.929 T - 4150.15 T^2 + 8890.76 T^3 , \\
a_3(T) &= -0.260076 + 8.92875 T - 60.868 T^2 + 136.57 T^3 , \\
a_4(T) &= 2.2663 - 8.30596 T + 49.3342 T^2 - 90.8501 T^3 , \\
a_5(T) &= 10.2955 - 317.077 T + 2412.15 T^2 - 6020.9 T^3 , \\
a_6(T) &= 3.12251 - 47.5277 T + 222.61 T^2 - 241.9 T^3 , \\
a_7(T) &= -3.39045 + 56.5927 T - 336.97 T^2 + 622.756 T^3 .
\end{aligned} \quad (\text{B4})$$

• $\rho\omega \rightarrow \gamma\pi$

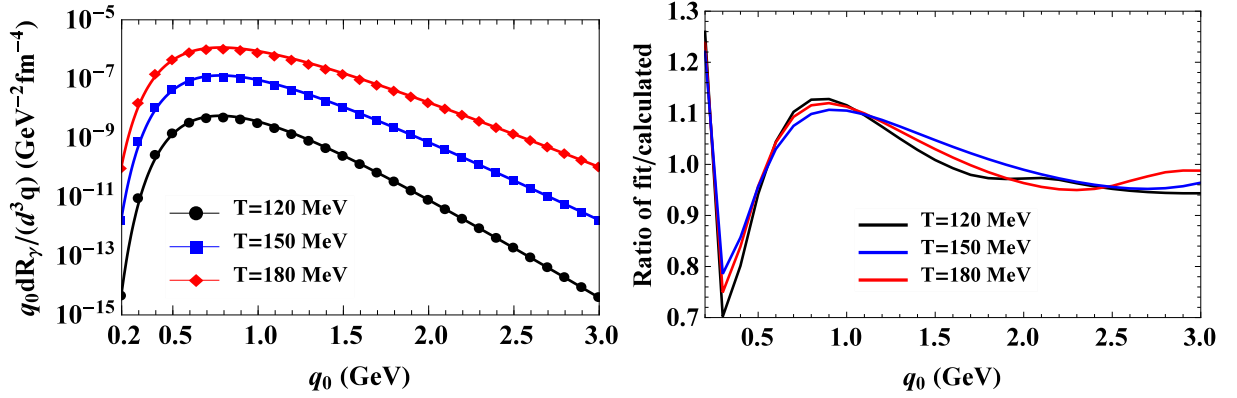


FIG. 16: Left panel: Calculated thermal photo-emission rates from the $\rho\omega \rightarrow \gamma\pi$ process (symbols) compared to the parametrized rates (lines). Right panel: Ratio of parametrized rates to calculated rates.

$$q_0 \frac{dR_{\rho\omega \rightarrow \gamma\pi}}{d^3q} = \exp \left[a_1 q_0 + a_2 + \frac{a_3}{(q_0 + 0.2)} + \frac{a_4}{(q_0 + 0.2)^2} \right] [\text{fm}^{-4} \text{GeV}^{-2}] , \quad (\text{B5})$$

$$\begin{aligned}
a_1(T) &= -29.6866 + 331.769 T - 1618.66 T^2 + 2918.53 T^3 , \\
a_2(T) &= -15.3332 + 90.2225 T - 300.185 T^2 + 428.386 T^3 , \\
a_3(T) &= -7.35061 + 109.288 T - 630.396 T^2 + 1227.69 T^3 , \\
a_4(T) &= -10.6044 + 109.1 T - 500.718 T^2 + 872.951 T^3 .
\end{aligned} \quad (\text{B6})$$

-
- [1] Y. Akiba *et al.*, arXiv:1502.02730 [nucl-ex].
[2] U. Heinz *et al.*, arXiv:1501.06477 [nucl-th].
[3] S. Borsanyi *et al.* [Wuppertal-Budapest Collaboration], JHEP **1009**, 073 (2010).
[4] A. Bazavov *et al.*, Phys. Rev. D **85**, 054503 (2012).
[5] R. Rapp, J. Wambach, and H. van Hees, in *Relativistic Heavy Ion Physics*, Landolt-Bornstein **23**, 134 (2010) [arXiv:0901.3289 [hep-ph]].
[6] C. Gale, in *Relativistic Heavy Ion Physics*, Landolt-Bornstein **23**, 445 (2010) [arXiv:0904.2184 [hep-ph]].
[7] J. Alam, Pramana **84**, 861 (2015).
[8] R. Rapp, Adv. High Energy Phys. **2013**, 148253 (2013).
[9] R. Arnaldi *et al.* [NA60 Collaboration], Eur. Phys. J. C **61**, 711 (2009).
[10] D. Adamova *et al.* [CERES Collaboration], Phys. Lett. B **666**, 425 (2008).
[11] F. Geurts [STAR Collaboration], Nucl. Phys. A **904-905**, 217c (2013).
[12] H. van Hees, C. Gale, and R. Rapp, Phys. Rev. C **84**, 054906 (2011).
[13] A. Adare *et al.* [PHENIX Collaboration], Phys. Rev. Lett. **104**, 132301 (2010).
[14] A. Adare *et al.* [PHENIX Collaboration], Phys. Rev. Lett. **109**, 122302 (2012).
[15] M. Wilde *et al.* [ALICE Collaboration], Nucl. Phys. A

- 904-905**, 573c (2013).
- [16] D. Lohner *et al.* [ALICE Collaboration], J. Phys. Conf. Ser. **446**, 012028 (2013).
- [17] C. Yang *et al.* [STAR Collaboration], Nucl. Phys. A (2014).
- [18] F. M. Liu, T. Hirano, K. Werner, and Y. Zhu, Phys. Rev. C **80**, 034905 (2009).
- [19] H. Holopainen, S. Räsänen, and K. J. Eskola, Phys. Rev. C **84**, 064903 (2011).
- [20] M. Dion *et al.*, Phys. Rev. C **84**, 064901 (2011).
- [21] P. Mohanty *et al.*, Phys. Rev. C **85**, 031903 (2012).
- [22] O. Linnyk, W. Cassing, and E. L. Bratkovskaya, Phys. Rev. C **89**, 034908 (2014).
- [23] A. Bzdak and V. Skokov, Phys. Rev. Lett. **110**, 192301 (2013).
- [24] C. Shen, U. W. Heinz, J. F. Paquet, and C. Gale, Phys. Rev. C **89**, 044910 (2014).
- [25] A. Monnai, Phys. Rev. C **90**, 021901 (2014).
- [26] H. van Hees, M. He, and R. Rapp, Nucl. Phys. A **933**, 256 (2014).
- [27] C. Gale *et al.*, Phys. Rev. Lett. **114**, 072301 (2015).
- [28] L. McLerran and B. Schenke, [arXiv:1504.07223 [nucl-th]].
- [29] J. Wess and B. Zumino, Phys. Lett. B **37**, 95 (1971).
- [30] E. Witten, Nucl. Phys. B **223**, 433 (1983).
- [31] S. Turbide, R. Rapp, and C. Gale, Phys. Rev. C **69**, 014903 (2004).
- [32] R. Rapp and C. Gale, Phys. Rev. C **60**, 024903 (1999).
- [33] L. D. McLerran and T. Toimela, Phys. Rev. D **31**, 545 (1985).
- [34] J. J. Sakurai, *Currents and Mesons*, The University of Chicago Press (Chicago, 1969).
- [35] H. A. Weldon, Phys. Rev. D **28**, 2007 (1983).
- [36] N. M. Kroll, T. D. Lee, and B. Zumino, Phys. Rev. **157**, 1376 (1967).
- [37] T. E. O. Ericson and W. Weise, *Pions and Nuclei*, Clarendon Press (Oxford, 1988).
- [38] J. I. Kapusta, P. Lichard, and D. Seibert, Phys. Rev. D **44**, 2774 (1991); Phys. Rev. D **47**, 4171 (1993).
- [39] K. A. Olive *et al.* [Particle Data Group Collaboration], Chin. Phys. C **38**, 090001 (2014).
- [40] J. I. Kapusta and C. Gale, *Finite-Temperature Field Theory: Principles and Applications*, Cambridge University Press (Cambridge, 2006).
- [41] J. e. Alam, P. Roy, S. Sarkar and B. Sinha, Phys. Rev. C **67**, 054901 (2003).
- [42] W. Liu and R. Rapp, Nucl. Phys. A **796**, 101 (2007).
- [43] M. Heffernan, P. Hohler, and R. Rapp, Phys. Rev. C **91**, 027902 (2015).
- [44] R. Rapp, H. van Hees, and M. He, Nucl. Phys. A **931**, 696 (2014).
- [45] M. Urban, M. Buballa, R. Rapp, and J. Wambach, Nucl. Phys. A **673**, 357 (2000).
- [46] R. Rapp and J. Wambach, Eur. Phys. J. A **6**, 415 (1999).